Materials & Design 221 (2022) 110946

Contents lists available at ScienceDirect

Materials & Design

journal homepage: www.elsevier.com/locate/matdes

In-situ X-ray tomographic imaging and controlled steering of microcracks in 3D nanopatterned structures

Kristina Kutukova [a], Jürgen Gluch [b,1], Matthias Kraatz [b], André Clausner [b], Ehrenfried Zschech [a,*]

[a] deepXscan GmbH, Zeppelinstr. 1, 01324 Dresden, Germany
[b] Fraunhofer Institute for Ceramic Technologies and Systems IKTS, Maria-Reiche-Str. 2, 01109 Dresden, Germany

HIGHLIGHTS

- A novel technique to monitor and control the microcracking process in specially designed 3D nanopatterned structures in real time is demonstrated on a technically relevant materials system, i.e. an on-chip interconnect stack. The three-dimensional details of the complicated physical failure mechanism are unveiled with high resolution.
- The combination of X-ray microscopy and micromechanics and the ability to image microcracks in a model system with a hierarchically structured architecture is described.
- The critical energy release rate at the crack tip is determined quantitatively in sub-100 nm regions.
- A controlled microcrack steering into regions with high fracture toughness is demonstrated for an engineered hierarchical materials system.

GRAPHICAL ABSTRACT

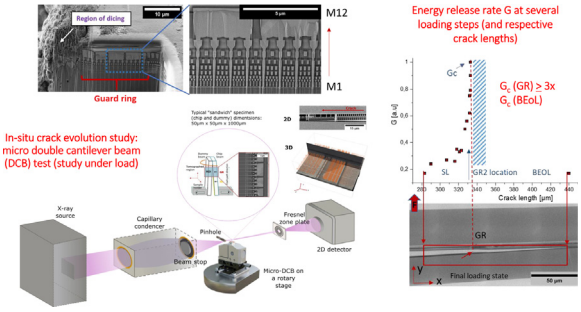

ARTICLE INFO

Article history:
Received 21 May 2022
Revised 8 July 2022
Accepted 11 July 2022
Available online 21 July 2022

Keywords:
X-ray computed tomograohy
X-ray microscopy
3D morphology
Micromechanical test

ABSTRACT

An experimental approach to control the fracture behavior of 3D nanopatterned structures in real time and to describe the microcrack propagation in solids quantitatively is presented. The three-dimensional details of the complicated failure mechanism are unveiled with high resolution using a method that integrates a micro-scale fracture mechanics test into a nano X-ray computed tomography system, to allow *in-situ* 3D imaging of the kinetics of damage mechanisms in integrated circuits. With the unique combination of a miniaturized micro-mechanical experiment and high-resolution X-ray imaging, the critical energy release rate at the crack tip of materials is determined quantitatively in sub-100 nm dimension, which allows to reveal scale-dependent mechanical properties. The ability of controlled microcrack steering in engineered materials and structures into regions with high fracture toughness is demonstrated. This unique characterization capability promises broad applications for design and

* Corresponding author.
E-mail address: ehrenfried.zschech@deepxscan.com (E. Zschech).
[1] New affiliation: Robert Bosch Semiconductor Manufacturing Dresden GmbH, Dresden, Germany.

https://doi.org/10.1016/j.matdes.2022.110946

Microcrack propagation and steering
Energy relase rate

manufacturing of robust microchips in future technology nodes, and it is applicable to the study of a broad variety of 3D nanostructured material systems.

1. Introduction

Nowadays, 100 years after Griffith's ground-breaking paper describing the fundamentals of fracture mechanics [1], the study of crack evolution in and failure of materials at micro- and nanoscale has become an important area of fundamental research with broad applications in industries [2,3]. The mechanistic study of how microcracks are formed, evolve, and interact with the surrounding materials and interfaces provides valuable insight into designing of defect-tolerant materials and structures. Successful examples range from natural biological materials such as bones and nacres [4] to artificial materials such as thin films, nanocomposites and engineered heterogeneous materials, e.g. toughened ceramics, thermo-mechanically processed alloys and porous materials for battery electrodes [5–7].

The continuous advancement of integrated circuit technology, well known as "Moore's law", is representing the cornerstone achievement of the semiconductor industry. On a square centimeter-size chip of advanced technology, tens of billions of transistors are fabricated and interconnected hierarchically as one integrated system. Modern microprocessors feature multilayered on-chip interconnects for power and signal distribution – a suitable example for 3D nanopatterned structures. From a material perspective, the interconnect stack represents a scientifically interesting model system of technological importance. As a hybrid composite consisting of hierarchically structured metal interconnect lines and vias embedded in interlayer dielectrics (ILD), structural complexity and material heterogeneity provide an appealing test bed for fundamental fracture mechanics concepts and approaches. From the technology and reliability perspectives, characterization and control of microcracks play a critical role in designing mechanically robust integrated circuits. For instance, microcracks can preexist as manufacturing defects within the active chip area, and those in high stress regions such as near die edge bumps can be triggered to propagate when they are subject to excessive chip-package interaction [8]. Microcracks can also be formed outside the active chip area during the wafer dicing process, and they can slowly grow inwards driven by thermo-mechanical stress and harsh environment, and eventually, they can find their way into the active die area causing functional or even catastrophic failure [9]. To reduce chip parasitic delay and power dissipation, ultralow permittivity (or ultralow-'k') dielectric materials, such as nanoporous organosilicate glass, are needed as ILD in on-chip interconnect stacks. Because of their molecular bonds and nanoporosity, ultralow-'k' materials are intrinsically brittle. Additionally, sensitivity to moisture-accelerated cracking is a serious concern. To protect the active chip area against cracking and at the same time to provide a hermetic seal against moisture and detrimental chemicals, metal guard ring (GR) structures surrounding the active die have been implemented in modern chip technology to arrest inward crack propagation [10]. However, without scaling, GRs will occupy an increasing fraction of the scaled die area, which will be increasingly costly for small die products and chiplets. A detailed characterization of the kinetic process causing failure and the identification of weak points are critical to adequately scale the GR structures without sacrificing their protective functionality. Stringent yield and reliability requirements have posed profound challenges on managing mechanical failures through fabrication as well as at service of modern microprocessor chips. While there are ample choices of established techniques for *post mortem* failure analysis, experimental methods that can provide real time monitoring and control of failure behavior in realistic integrated circuits with 3D nanopatterned structures are limited in resolution and applicability. Here we present a method that integrates high-resolution X-ray imaging with micro-scale fracture mechanics. Transmission X-ray microscopy (TXM) and nano X-ray computed tomography (nano-XCT) provide desirable and unique information that complement other established techniques widely used in physical failure analysis labs, such as scanning electron microscopy (SEM) and transmission electron microscopy (TEM). SEM provides mainly surface information and TEM requires extremely thin samples, which limits their use in real time and non-destructive applications. In contrast, TXM and nano-XCT allow a nondestructive visualization of defects such as microcracks in materials with high spatial resolution, and they are applicable for significantly larger sample volumes without modifying the stress state in the region of interest. The capability to image in real time defect evolution processes such as microcrack propagation in realistic integrated circuits provides the opportunity to reveal failure mechanisms with important details, i.e. information that is usually missing from *post mortem* inspection [11,12].

2. Method: Imaging of microcrack propagation in 3D nanopatterned structures

2.1. Miniaturized fracture mechanics test in the X-ray microscope

In this paper, we demonstrate the capability of *in-situ* X-ray imaging and steering of microcrack propagation in integrated circuit structures – as an example for 3D structured materials and systems - by combining nano-XCT with a quantitative micro fracture mechanics test. With this unique combination, the critical energy release rate at the crack tip of materials can be determined quantitatively in sub-100 nm dimension, and microcracks can be steered in a controlled way. We choose the on-chip interconnect and GR structures on a leading-edge microprocessor chip as model system to illustrate this unique capability.

We designed and built a miniaturized micro-double cantilever beam (micro-DCB) test setup that is compatible with a commercial laboratory X-ray microscope (Xradia nanoXCT-100) to conduct a small-scale fracture test and to simultaneously visualize the evolution of the microcrack under load nondestructively [11,12]. The working principle is illustrated in Fig. 1a. The X-ray microscope is equipped with a rotating anode X-ray source operating at 8 keV (Cu-Kα), a polycapillary condenser optics, a Fresnel zone plate, and a scintillation detector with CCD camera [13–16]. A spatial resolution of approximately 100 nm can be achieved in the current laboratory setup as determined using a Siemens star test structure; even higher resolution of 20 nm has been demonstrated using synchrotron radiation [17].

A micro-DCB sample is prepared from a microprocessor wafer with 12 levels of on-chip interconnects manufactured in an industry fab at an advanced technology node. The area of interest is at the proxy of die edge that consists of the on-chip interconnect stack, the protective GR structure and the scribe line area that is reserved for wafer dicing. A small beam is cut out of the wafer and glued together with a dummy silicon beam. The resulting sandwich sample is sawed and polished to a rod with a length of

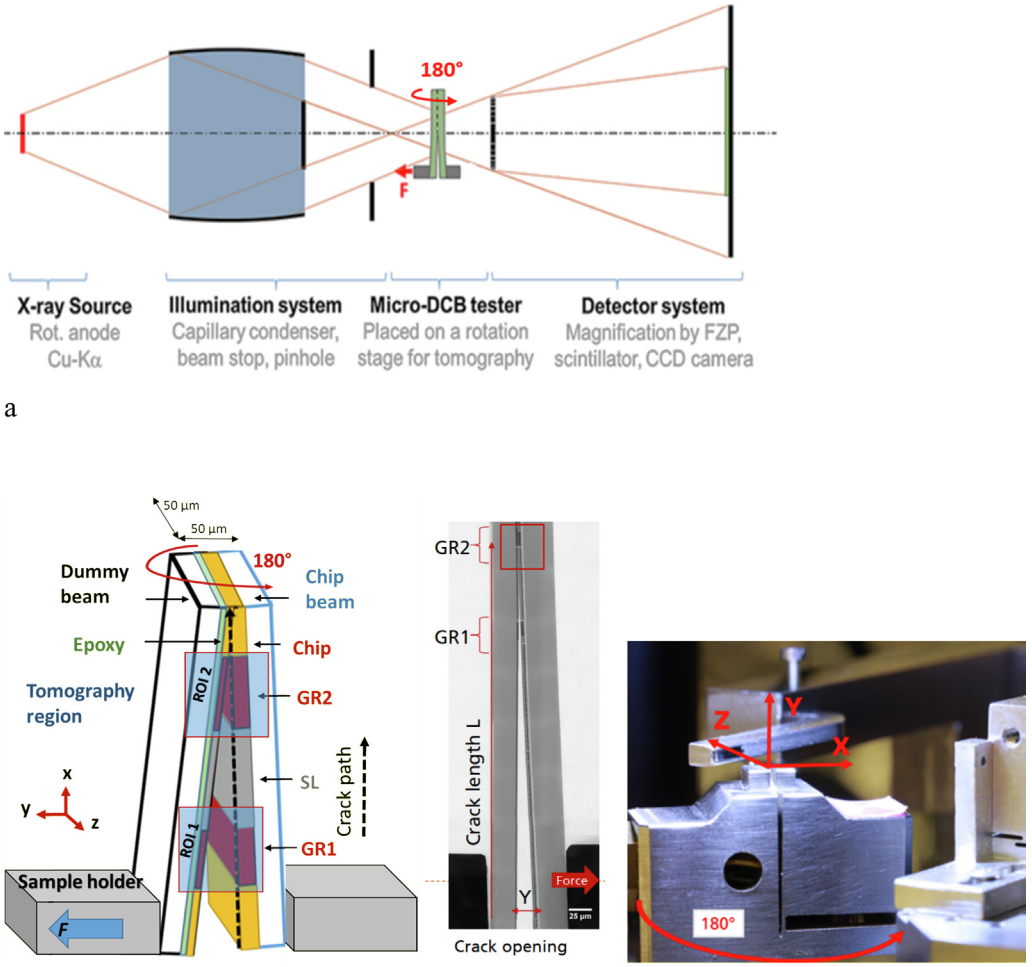

Fig. 1. a) Scheme of the experimental setup: micro-DCB test in a laboratory full-field transmission X-ray microscope, b) Scheme of the micro-DCB test using a sandwich sample with the ROI, the on-chip interconnect stack of a microchip featuring two copper guard ring structures (GR1 and GR2) separated by a scribe line (SL), and respective radiograph, c) photograph of the micro-DCB test setup inside the X-ray microscope.

approximately 1 mm and with a cross-section of 50 µm by 50 µm to be transparent to 8 keV X-ray photons – see Fig. 1b. To facilitate crack initiation and to simulate wafer dicing induced damage, a pre-crack is introduced in the scribe line area by inserting a razor blade at the interconnects structure near the glue bonding interface. The thickness ratio of the sample beam to the dummy silicon beam can be varied to tune the fracture mode at the crack tip, which provides an effective knob to control the crack propagation behavior.

The micro-DCB sample is mounted on a rotation stage and aligned with the crack front parallel to the optical axis of the X-ray microscope for imaging and tomography data collection [11]. The miniaturized, piezo-driven micro-DCB test setup (see Fig. 1c) imposes incremental displacements in steps of 50 nm to gradually pull the sample apart. The setup is designed to allow the entire sample to be imaged at arbitrary rotation angles without shadowing by the fixture.

2.2. Determination of the local energy release rate

The standard double cantilever beam (DCB) test is one of the most common experimental techniques for the determination of the critical energy release rate G_c of macroscopic specimens with plane interfaces. A typical DCB test geometry is schematically shown in Fig. 2. This scheme includes the geometric measures of a partially delaminated sandwich sample and it indicates the force introduction points. In both, the macroscopic and the microscopic DCB geometries, a force F is applied perpendicular to the interfacial

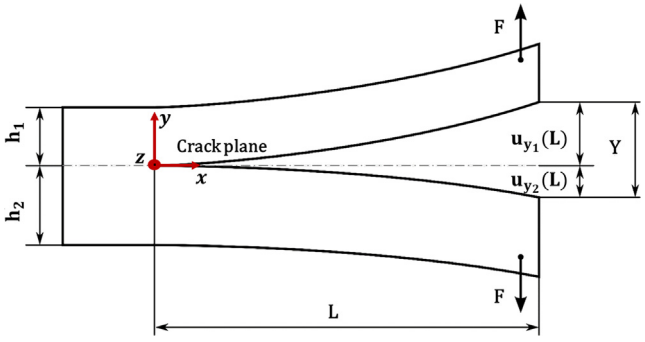

Fig. 2. Illustration of a partially delaminated standard DCB sample with freely rotatable beam ends at the force introduction points: F – applied force, h_1 and h_2 – beam heights, $u_{y_n}(L)$– cantilever deflections at the end of the beam in y {n = 1,2}, Y = $u_{y_1}(L)$ + $u_{y_2}(L)$ - maximum beam opening, x – coordinate in interface/crack plane direction with origin at the crack tip, y – coordinate perpendicular to the interface/crack plane, L – crack length.

plane of the DCB sample to create an interfacial crack with a length L and a crack opening Y (sum of both single beam deflections $u_{y_n}(L)$ {n = 1,2}) at the sample mount position × = L (x = 0 at crack tip). For a symmetric double beam geometry, it results in a pure normal force crack opening, the so-called fracture mode I. However, geometric inaccuracies of the sample, i.e. deviations from a symmetric micro-DCB sample, result in asymmetric bending of the beams. Such inaccuracies are more pronounced in the micro-DCB test. Additionally, non-symmetry can also be applied intentionally to steer the crack to tough regions in multi-layered stacks in a controlled way. This non-symmetry causes an additional shear component in the crack driving forces (mixed modes I and II). As a consequence, the determination of the single beam deflections $u_{y_n}(L)$ becomes important.

For the micro-DCB geometry used in this study, the single beam deflections $u_{y_n}(L)$ and other experimental parameters are not directly accessible from the measured data. To determine these experimentally not accessible parameters, the Euler-Bernoulli bending beam differential equation was applied. More precisely, a micro-DCB adapted solution of the Euler-Bernoulli equation was fitted to the bending lines of the two cantilevers based on radiographs. In the case of small deflections, which is a reasonable assumption for the micro-DCB geometry, the shape of the two bending cantilevers can be described by the Euler-Bernoulli differential equation.

$$q = \frac{d^2}{dx^2}\left(EI\frac{d^2u}{dx^2}\right) \tag{1}$$

where q is a distributed load (in N/m^2), E is the Young's modulus (in Pa), $I = I_{zz}$ is the second moment of area (in m^4) for a bending around the out of plane coordinate z (called just I in the following), and $u(x)$ is the beam transverse displacement in y direction at the position ×, called the bending line. The term $\frac{d^2u}{dx^2}$ (or short ú) is the second derivative of the beam deflection. Often the material property E and the geometry parameter I are constant, and consequently, the product EI, which is called flexural rigidity, is also constant.

For the micro-DCB geometry, the fixed end of the Euler-Bernoulli beam was chosen at the crack tip position which is defined as x = 0. There, the deflection u(x = 0) and the slope u'(x = 0) are zero. At the force introduction point, at the beam length x = L, the boundary conditions for the micro-DCB geometry deviate from those for the standard DCB geometry. The main differences are the boundary conditions in the bending slopes u'(x) and bending moments M(x) at × = L. For the standard DCB geometry, the beam is free to move at × = L, the bending moment is zero at this point, and the slope adjusts to a value of non-zero accordingly. For the micro-DCB geometry, the beam end at the force introduction points is fixed due to the sample mounting using gluing. A fully fixed beam would lead to boundary conditions of u'(x = L) = 0, and the bending moment would be non-zero. In reality, the boundary conditions at x = L of the micro-DCB are between these extremes, i.e. u'(x = L) as well as M(x = L) are non-zero. To consider these boundary conditions, a parameter A is introduced that describes the amount of fixture at the beam ends at x = L. The value A is in the range of $0.5 \leq A \leq 1$ with the extremes A = 0.5 for u'(x = L) = 0 and A = 1 for M(x = L) = 0. The two extreme cases of the micro-DCB test, i.e. "fixed beam ends" and "free beam ends", and the respective geometrical parameters A are shown schematically in Fig. 3. The parameter A is a parameter that is introduced to describe the boundary conditions of the beams (first derivative of the bending line) at the displaced cantilever ends, affecting the bending moment of the beam. Solving the differential equation (1) for the two extreme cases "free beam end" and "fixed beam end" results in A = 1 for a free beam end and in A = 0.5 for a fully

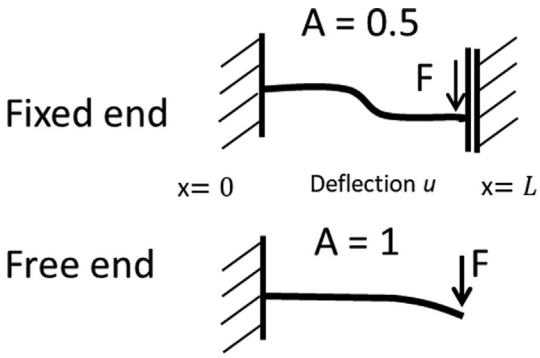

Fig. 3. Scheme for two extreme cases, fixed cantilever ends and free cantilever ends.

constrained beam with a zero slope at the beam end. The values for the parameters A_1 and A_2 (for the two cantilevers) were determined from the real bending line determined from radiographs, applying a least-square fitting procedure based on the micro-DCB adapted Euler-Bernoulli beam model. Since there is an inflection point in the bending line, two parameters can be determined from the cubic fit, i.e. the applied force F and the parameter A. That means, for the steady state (no crack propagation), it is possible to fully parameterize the Euler-Bernoulli model and to determine the potential (elastic) energy for the different loading steps of each cantilever. These A and F values are used for the calculation of the energy release rate for crack propagation at the respective loading conditions [cp. Eq. (11)].

To solve the bending beam differential equation, a stepwise integration and boundary condition implementation is applied. As a result, a relationship between the applied force F, the bending line shape, and the resulting beam deflections u_{y_n} (n = 1, 2) for the two uniform beams of the micro-DCB experiment is derived:

$$u_{y_n}(x) = -\frac{Fx^3}{6EI_n} + \frac{A_nFLx^2}{2EI_n} \tag{2}$$

The Euler-Bernoulli beam model, which is valid for beams under the assumptions that the beam cross-section dimensions are small compared to the beam length (equals crack length here) and that the constrained beam ends at the support side (crack tip here) are horizontally oriented, is applied to the two micro-DCB cantilevers for the determination of the stored elastic energy and ultimately of the energy release rate for crack propagation. The geometric sizes in a real micro-DCB sample are indicated in stitched radiographs in Fig. 4.

The energy release rate G is the normalized amount of elastic energy U_{el} stored in the system, which will be released if the crack with a length × propagates, can be expressed in the following equation:

$$G = -\frac{1}{b}\frac{dU_{el}}{dx}, \tag{3}$$

with b being the sample width. The critical energy release rate G_c that it needed for crack growth can be determined by the condition that the external energy is equal to the stored elastic energy. That means, crack growth is initiated if the energy release rate is larger than a critical value G_c, i.e. $G > G_c$. The external energy needed for crack propagation U_{el} can be calculated by integration the applied force F up to the maximum beam deflection $u_{\bar{y}}(L)u_{y_n}(L)$:

$$U_{el} = \int_0^{u_{y_n}(L)} F(x)dx \tag{4}$$

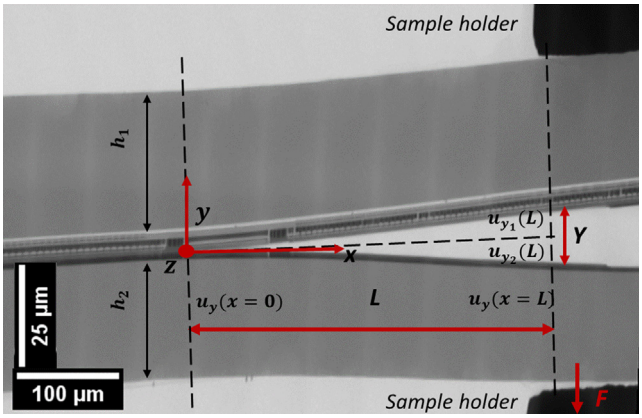

Fig. 4. Stitched radiographs of a micro-DCB sample. The stitching array of 3 × 12 radiographs is compressed along the × coordinate for better visualization of the geometric sizes.

The force equation is found from Eq. (2):

$$F = \frac{6EIu_{y_n}(x)}{x^3 - 3A_nLx^2} \tag{5}$$

Considering this energy equation, the following result is derived for each cantilever, i.e. for {n = 1,2}:

$$U_{el,n} = \frac{3EIu_{y_n}(L)^2}{L^3(3A_n - 1)} \tag{6}$$

Inserting Eq. (6) into Eq. (3) and considering that the second moment of inertia of the beam's rectangular cross-section is $I = b^*h^3/12$, with b, h_n - width and height of cantilever n {n = 1,2}, G_n for one cantilever can be written:

$$G_n = \frac{3Ehn^3u_{y_n}(L)^2}{4L^4(3A_n - 1)} \tag{7}$$

Consequently, the G_c value for the crack propagation in the micro-DCB test is the sum of the contributions for the two beams.

$$G_c = \sum_1^{n=2} \frac{3Eh_n^3u_{y_n}(L)^2}{4L^4(3A_n - 1)}.G_{DB} = G_{B_1} + G_{B_2} \tag{8}$$

The beam deflections can be expressed by simple algebraic relationships between the measurable geometric parameter $Y = u_{y_1}(L)+u_{y_2}(L)$, h_1 and h_2 (see Fig. 3) and beam ratio $= \frac{h_1}{h_2}$ $e = \frac{h_1}{h_2}$:

$$u_{y_1}(L) = \frac{Y}{(e^3 + 1)} \tag{9}$$

$$u_{y_2}(L) = \frac{e^3Y}{(e^3 + 1)}. \tag{10}$$

Finally, the G_c value for the crack propagation in the micro-DCB experiment, taking into account the parameters A_1 and A_2 and the beam ratio e results in:

$$G_c = \frac{3Eh_1^3Y^2}{4L^4(e^3 + 1)^2}\left(\frac{1}{(3A_1 - 1)} + \frac{e^3}{(3A_2 - 1)}\right) \tag{11}$$

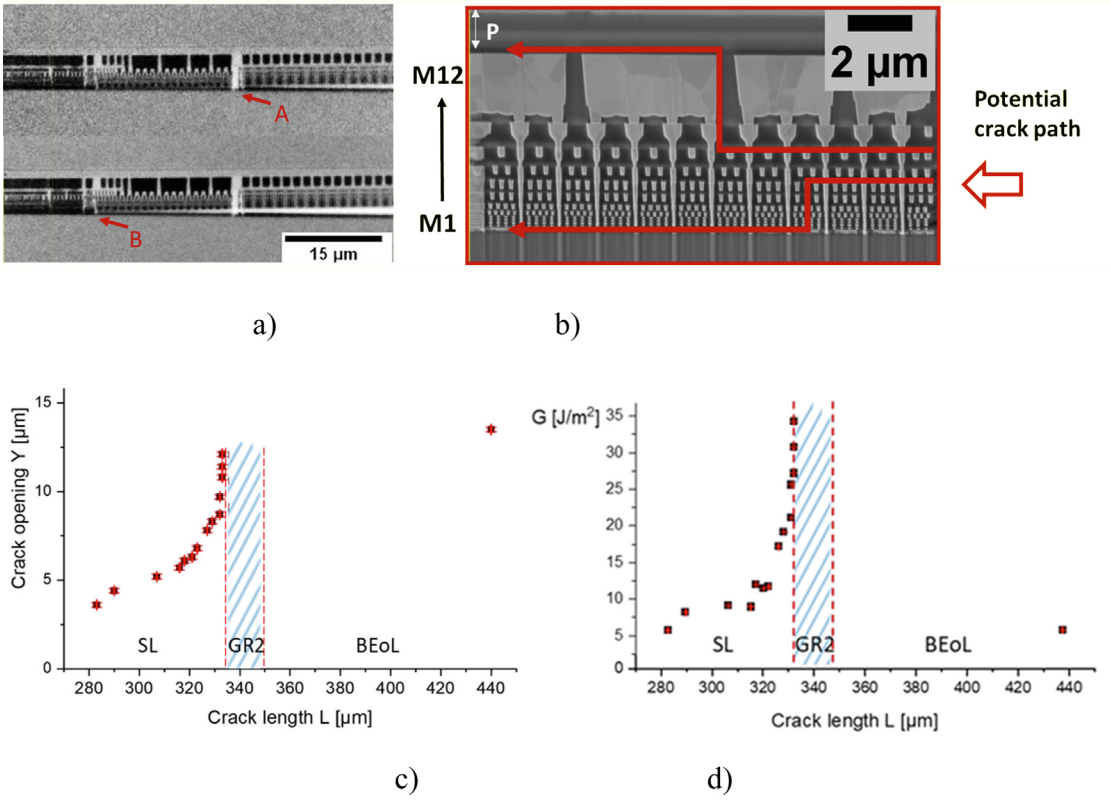

Fig. 5. a) Radiographs of the micro-DCB sample with an acquisition time interval of 15 s at two different loading states: crack tip propagating from right to left firstly towards GR2 (A) and finally in GR2 (B), b) SEM cross-section image of the GR structure with 12 metallization (M1 - M12) layers and a post passivation layer on top, and two schemes for potential paths of microcracks propagating from right to left (red lines). Mn refers to the *n*-th metallization layer, P to the post passivation layer, c) Crack opening Y and d) energy release rate G vs crack length L at several loading steps during the micro-DCB test. (For interpretation of the references to color in this figure legend, the reader is referred to the web version of this article.)

The critical energy release rate decreases with L^{-4} if the crack propagates in a controlled way.

3. Results and discussion

3.1. Critical energy release rate at the crack tip

Radiographs of a microcrack as it approaches and passes the GR of the micro-DCB sample are shown in Fig. 5a. From the tomography data, test structure and microcrack are reconstructed to reveal the three-dimensional details of the kinetic process that causes damage and failure. Depending on the pre-cracking location and the mode mixity, microcrack propagation can be related to certain metal levels among the multiple potential paths, as schematically illustrated in the SEM cross-section image of a GR structure in Fig. 5b. In this particular example, the beam thickness ratio is approximately 1.3:1, and the cracking path is along the lower metallization layer (M1). Geometrical information of the microcrack including crack length and crack tip opening displacement is extracted since these values are needed for the quantitative determination of the local energy release rate at the crack tip. As the crack front approaches the GR structure, the crack opening is increasing gradually, and the crack growth rate is slowing down, as shown in Fig. 5c and Fig. 5d. Once the crack tip reaches the GR, it is stopped completely by the outermost GR that is made of primarily copper with a thin diffusion barrier. The ductility of Cu helps blunt the crack tip and provides toughness to retard crack propagation. The crack tip opening increases sharply and the strain energy builds up while the crack length remains constant. When the crack tip opening increases to 12.1 μm, the energy release rate reaches the critical value of 34.8 J/m^2, at which catastrophic failure of the GR occurs. This critical energy release rate provides a measure of fracture resistance of the GR structure against inward crack propagation. It is significantly higher than the respective value in the SL and in the BEoL stack. We note that the mechanics model developed in this study accounts for the geometric imperfection of the sample and the specific clamping boundary condition of the micro-DCB specimen due to the finite sample length relative to the clamping part.

The real-time monitoring of crack propagation provides invaluable insight to the failure mechanism and directions to optimize the GR design. That means, once the outermost GR (GR1) is broken through, the crack cannot be arrested by the remaining GRs in the current design, and eventually damage to the functional interconnect structure can occur. To understand this failure behaviour, finite element analysis, particularly 2D static calculation of the energy release rate as a function of crack length, was conducted. The result shows that the energy release rate, which is the fracture driving force, increases with longer crack length, while the fracture resistance is constant as determined by the GR materials and dimension. Therefore, an even distribution of identical GRs is not the most efficient way to stop crack penetration. Only the real-time imaging capability – and not conventional *post mortem* analysis – can reveal the critical role of the outermost GR.

3.2. Controlled microcrack steering

The understanding of the crack path selection under different boundary conditions is critical for the design of GR structures to better protect the microchip against damage caused by inward cracking from chip edges and corners. In particular, the local energy release rate along the chip edge is location- and product-dependent. In the micro-DCB test, we tune the fracture mode at the crack tip to envelop, to a significant extent, the boundary conditions experienced by the chip edge under realistic reliability test and service conditions with the goal to understand their effect on the crack path selection. The mode mixity at the crack tip characterizes the relative significance of mode-I(opening) and mode-II (shear) components of the fracture driving force, the ratio of them defines the angle of mode mixity. Finite element analysis [18] demonstrates that the global mode-mixity angle can be adjusted from zero to approximately 38° varying the mode mixity within the range of –23° to 23° by changing the beam thickness ratio from 0.5 to 2 from one in the micro-DCB test. From the geometry and the boundary conditions, the global mode mixity can be calculated using finite element analysis as reported in [9] for asymmetric DCB sample geometries as a function of beam thickness. The mode mixity plays an important role in determining the path selection of a propagating crack. For each condition multiple tests were conducted to characterize the reproducibility and sensitivity. With the 3D model reconstructed from the XCT data, the cracking path was determined by a "virtual" cross-section through the region of interest without having to physically cut the sample apart.

Depending on the mode-mixity, the microcrack behavior is more complex inside the multi-level integrated structure than for blanket film stacks or single-level interconnects studied previously [9,18]. As one example, Fig. 6 shows a "virtual" cross-section at the final loading stage for a nearly symmetric configuration, i.e. the thickness ratio e = h_1/h_2 of the dummy beam h_1 and the microchip beam h_2 are targeted to be equal with vanishing mode mixity. Due to sample preparation imperfection, the equality of beam thickness is approximate. Note that the 3D data set is presented in XY plane projection perpendicular to the metallization layers, and the "vir-

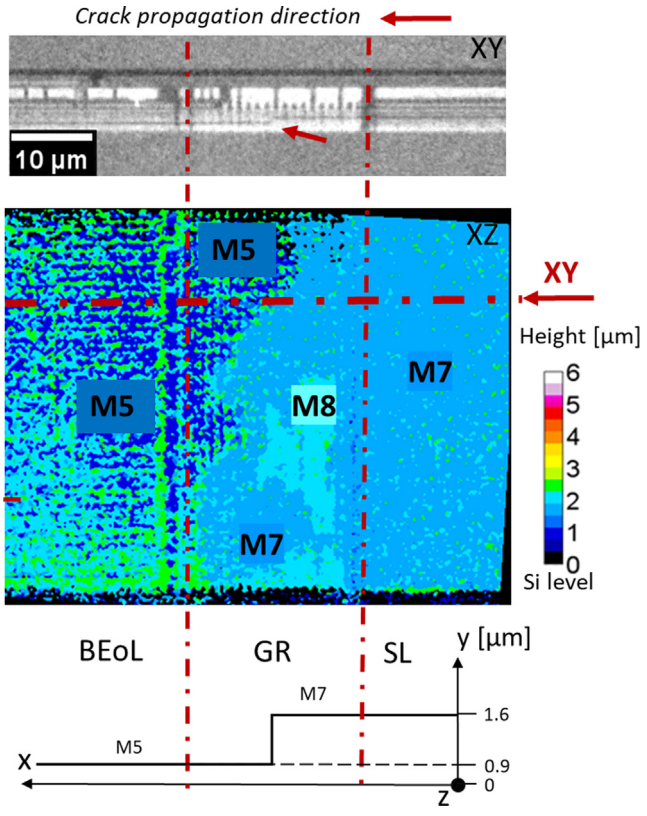

Fig. 6. Virtual cross-section (XY view) with indicated crack path change from M7 to M5 (top); XZ height map of the crack in the on-chip interconnect stack (SL, GR, Cu/low-k BEoL), heights above the Si substrate indicated by colors (middle); Scheme of the cross-section XY at the indicated z location (red line) with crack pathway, showing crack path change from M7 to M5, heights above the Si substrate in μm (bottom). The color scale bar corresponds to the heights from zero (Si substrate) to about 6 μm (post passivation layer P). (For interpretation of the references to color in this figure legend, the reader is referred to the web version of this article.)

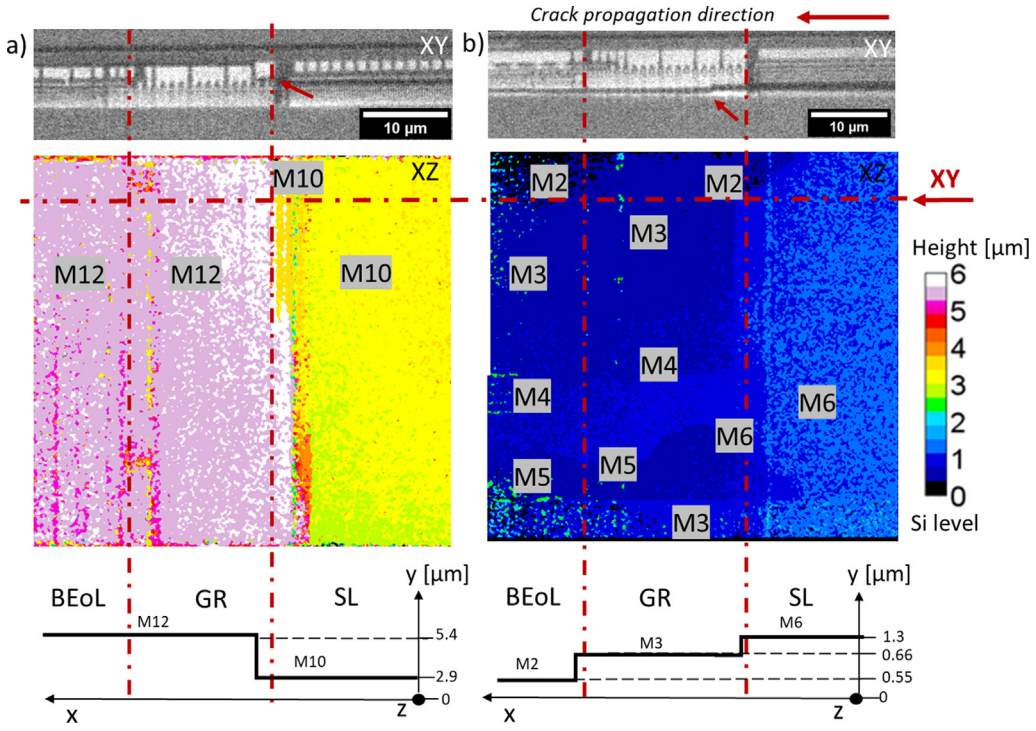

Fig. 7. Virtual cross-sections (XY views) with indicated crack path changes (top); XZ height maps of the crack in the on-chip interconnect stack (SL, GR, Cu/low-k BEoL), heights above the Si substrate indicated by colors (middle); Schemes of the cross-section XY at the indicated z location (red line) with crack pathways, showing crack path changes from M10 to M12 (a) and M6 via M3 to M2 (b), heights above the Si substrate in µm (bottom). (For interpretation of the references to color in this figure legend, the reader is referred to the web version of this article.)

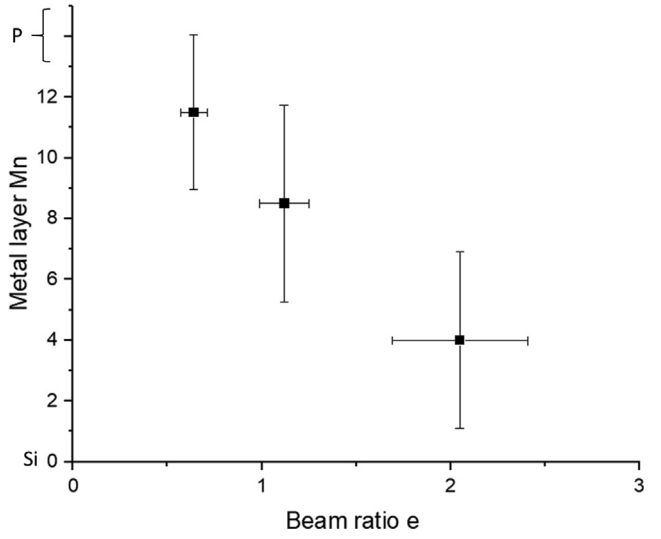

Fig. 8. Dominant metal layers of crack propagation for several beam height ratios e, based on 7 samples for e ≈ 0.5, 9 samples for ≈ 1, and 12 samples for e ≈ 2, error bars from statistical data analysis.

tual" cross-section is the XZ horizontal map with heights indicated by colors. The plot shows that, after pre-cracking, the microcrack starts to propagate from the scribe line area (SL) at the M7 layer towards the GR structure. After penetrating the first GR, part of the crack front kinks into M8 for a short distance before returning to M7, while the rest of the crack front remains propagating along M7. We believe the short excursion along M8 is due to local perturbation. Eventually, the microcrack is penetrating the full GRs and seek path along M5 in the active interconnect stack where the metal density is reduced compared to M7. The Fig. 6 bottom panel shows the schematic crack path for one particular z position, with crack path following along M7 and subsequently transitioning to M5; the transition point is marked by a red arrow in the Fig. 6 top panel. The full 3D details of the specific crack paths and the sequence of microcrack propagation underline importance and effectiveness of the nondestructive 3D imaging technique presented here.

Fig. 7 shows virtual cross-sections of asymmetric micro-DCB specimens at the final loading stage, with e = 0.65 (h_1 = 25 µm, h_2 = 38 µm) and e = 2.10 (h_1 = 40 µm, h_2 =19 µm), respectively. Due to the asymmetric sample geometries, the crack tip mode mixity has a substantial mode-II component with a mode angle close to ± 23° respectively. In contrast to the symmetric case, the imposed mode mixity drives the crack path upward from M10 to M12 in the case of e = 0.65, and downward from M6 to M3 and further to M2 in the case of e = 2.10 for this sample.

To analyze the statistical distribution and the sensitivity of the crack path selection, multiple repeats were conducted for each sample geometry configuration (symmetric vs asymmetric cases), and nano-XCT data sets were generated as described above. The crack pathways were analyzed based on the 3D tomography data set for each sample and summarized in Fig. 8. The data shows the clear effect of mode mixity on the crack path selection. That means, despite the spread of the initiation layer due to pre-cracking, microcracks tend to kink predominantly to upper metallization layers for e < 1, and predominantly to lower metallization layers for e > 1. At the same time, initiation location, local metal density and toughness at each metallization layer collectively contribute to determine the eventual crack path selection.

4. Summary

The capability to steer microcrack propagation in a controlled way with real time observation provides a powerful tool to study

the crack behavior inside the complex integrated circuit structure at different boundary conditions, as for different product and packaging technologies and for different temperature conditions. As one example, the learning can help to refine the GR design to a targeted drive and arrest of the crack with upper metallization where the Cu plasticity is toughening the region due to size effects [19], thus providing a structural component to stop crack propagation. Such a toughening strategy may prove invaluable for downscaling the footprint of GR structure without sacrificing the protective efficacy.

In this study, we present a method to achieve *in-situ* high resolution 3D imaging and steering of microcrack propagation for realistic microchip structures by integrating a micro-DCB test setup into a nano-XCT tool. For purpose of demonstration of the role of materials design for a technically relevant 3D nanopatterned structures, the process of guard ring damage by inward crack penetration under several mode mixity conditions has been studied with full three-dimensional details captured. A refined mechanics model has been developed to extract the critical fracture resistance of the GR structure in sub-100 nm dimension quantitatively from the nano-XCT and micro-DCB data, accounting for the specific sample geometry and clamping conditions. In addition, the ability of controlled microcrack steering into regions with high fracture toughness – i.e. with larger metal structures in microchips - is demonstrated.

The experimental setup and the approach of a quantitative data analysis provide an essential increase in knowledge for solid-state physics and fracture mechanics in small dimensions. We anticipate that this capability can find broad applications in other areas of semiconductor technology development, and more broadly in the design of engineered structural and functional materials with tailored micromechanical properties.

Data availability

Data will be made available on request.

Declaration of Competing Interest

The authors declare that they have no known competing financial interests or personal relationships that could have appeared to influence the work reported in this paper.

Acknowledgement

The authors thank Yvonne Standke and Zhongquan Liao, both Fraunhofer IKTS Dresden, Germany, for sample preparation and the TEM study, and Paul S. Ho, University of Texas, Austin/TX, USA, for helpful discussions. This work is funded by SRC under Member-Specific Research Contract No. P30697.

Appendix A. Supplementary material

Supplementary data to this article can be found online at https://doi.org/10.1016/j.matdes.2022.110946.

References

[1] A.A. Griffith, The phenomena of rupture and flow in solids, Philosophical Transactions of the Royal Society of London Series A 221 (1921) 163–198.
[2] R. Pippan, S. Wurster, D. Kiener, Fracture mechanics of micro samples: fundamental considerations, Mater. Des. 159 (2018) 252–267.
[3] J. Ast, M. Ghidelli, K. Durst, M. Goeken, M. Sebastiani, A.M. Korsunsky, A review of experimental approaches to fracture toughness evaluation at the micro-scale, Mater. Des. 173 (2019) (2019) 107762.
[4] A. Ghazlan, T. Ngo, P. Tan, Y.M. Xie, P. Tran, M. Donough, Inspiration from Nature's body armours - A review of biological and bioinspired composites, Compos. Part B Eng. 205 (2021) 108513.
[5] J.P. Oliviera, Z. Zeng, T. Omori, N. Zhou, R.M. Miranda, F.M. Braz Fernandes, Improvement of damping properties in laser processed superelastic Cu-Al-Mn shape memory alloys, Mater. Des. 98 (2016) 280–284.
[6] X. Zhu, Y. Chin, H. Chen, W. Luan, The diffusion induced stress and cracking behaviour of primory particle for Li-ion battery electrode, Int. J. Mat. Sci. 178 (2020) 105608.
[7] D. Tovar-Vargas, E. Roitero, M. Anglada, E. Jiménez-Piqué, H. Reveron, Mechanical properties of ceria-calcia stabilized zirconia ceramics with alumina additions, J. Europ. Cer. Soc. 41 (11) (2021) 5602–5612.
[8] W. Chu, T. Jiang, P.S. Ho, Effect of wiring density and pillar structure on chip packaging interaction for mixed-signal Cu low-k chips, IEEE Trans. Dev. Mater. Reliab. 21 (3) (2021) 290–296.
[9] H. Li, M. Kuhn, Controlled fracture and mode-mixity dependence of nanoscale interconnects, IEEE Trans. Dev. Mater. Reliab. 17 (4) (2017) 636–642.
[10] M.A. Rabie, N.A. Polomoff, S. Pozder, Optimizing die corner and optical groove corner crackstop support structures for mitigating dicing and CPI risks", in: IEEE 71st Electronic Components and Technology Conference (ECTC), 2021, pp. 1391–1398.
[11] K. Kutukova, S. Niese, J. Gelb, R. Dauskardt, E. Zschech, A novel micro-double cantilever beam (micro-DCB) test in an X-ray microscope to study crack propagation in materials and structures, Mater. Today Commun. 16 (2018) 293–299.
[12] K. Kutukova, S. Niese, C. Sander, Y. Standke, J. Gluch, M. Gall, E. Zschech, A laboratory X-ray microscopy study of cracks in on-chip interconnect stacks of integrated circuits, Appl. Phys. Lett. 113 (2018) 091901.
[13] A. Tkachuk, F. Duewer, H. Cui, M. Feser, S. Wang, W. Yun, X-ray computed tomography in Zernike phase contrast mode at 8 keV with 50-nm resolution using Cu rotating anode X-ray source, Zeitschrift für Kristallographie - Crystalline Materials 222 (2007) 650–655.
[14] F. Berto, A. Campagnolo, Three-dimensional effects on cracked components under anti-plane loading, Frattura ed Integrità Strutturale 9 (2015) 17–24.
[15] E. Zschech, M. Loeffler, P. Krueger, J. Gluch, K. Kutukova, I. Zglobicka, J. Silomon, R. Rosenkranz, Y. Standke, E. Topal, Laboratory computed X-ray tomography – a nondestructive technique for 3D microstructure analyis of materials, Practical, Metallography 55 (2018) 539–555.
[16] C. Jacobsen, X-ray Microscopy, Cambridge University Press, 2019.
[17] K. Kutukova, Z. Liao, S. Werner, P. Guttmann, Y. Standke, J. Gluch, G. Schneider, E. Zschech, In-situ X-ray Microscopy of Crack-Propagation to Study Fracture Mechanics of On-Chip Interconnect Structures, MRS Advances 3 (39) (2018) 2305–2310.
[18] H. Li, M.J. Kobrinsky, A. Shariq, J. Richards, J. Liu, M. Kuhn, Controlled fracture of Cu/ultralow-k interconnects, Appl. Phys. Lett. 103 (2013) 2319001.
[19] J.R. Greer, J.T.M. De Hosson, Plasticity in small-sized metallic systems: intrinsic versus extrinsic size effect, Prog. Mater. Sci. 56 (2011) 654–724.